nature communications

DG9 boosts PMO nuclear uptake and exon skipping to restore dystrophic muscle and cardiac function

Md Nur Ahad Shah [1], Harry Wilton-Clark[1], Farhia Haque[1], Brooklynn Powell[1], Laura Edellein Sutanto[1], Radha Maradiya [1], Pavel Zhabyeyev [2], Rohini Roy Roshmi [1], Saeed Anwar [1], Tejal Aslesh [1], Kenji Rowel Q. Lim [3], Rika Maruyama[1], Anne Bigot [4], Courtney S. Young[5], Scott Bittner[6], Melissa J. Spencer [5], Hong M. Moulton [6], Gavin Y. Oudit[2,7] & Toshifumi Yokota [1,8] ✉

Duchenne muscular dystrophy (DMD) is a severe neuromuscular disorder caused by DMD gene mutations, leading to the loss of functional dystrophin. While antisense oligonucleotide (ASO)-mediated exon skipping offers therapeutic potential, its efficacy in cardiac muscle remains limited. Here, we investigate DG9, a cell-penetrating peptide derived from human polyhomeotic 1 homolog (Hph-1) transcription factor, as an enhancer of phosphorodiamidate morpholino oligomer (PMO)-based therapy targeting exon 44. In a humanized DMD mouse model (h*DMD*del45;*mdx*), DG9-PMO significantly increases exon skipping, restores dystrophin expression, and improves muscle function, particularly in the heart. Mechanistically, DG9-PMO enhances intracellular uptake through multiple endocytic pathways and achieves superior nuclear localization. Compared to the benchmark R6G peptide, DG9-PMO exhibits greater efficacy in cardiac tissue with no detectable toxicity. These findings highlight DG9-PMO as a promising next-generation exon-skipping therapy with potential clinical relevance for improving both skeletal and cardiac outcomes in DMD patients.

Duchenne muscular dystrophy (DMD) is an X-linked neuromuscular disorder affecting 1 in 5000–6000 males every year[1]. This disease is caused by mutations in the *DMD* gene that result in the absence of dystrophin protein. Dystrophin is a membrane-bound protein responsible for stabilizing the sarcolemma by connecting the actin cytoskeleton to the extracellular matrix[2,3]. Absence of this protein results in myofiber degeneration and loss of ambulation followed by cardiorespiratory complications that lead to eventual death. While the recent advances in care and management guidelines can significantly increase the life expectancy of patients, cardiomyopathy emerges as a leading cause of mortality in DMD patients, underscoring the urgent need for therapies that can effectively target both skeletal and cardiac muscles[4,5].

Antisense oligonucleotide (ASO)-mediated exon skipping is a promising therapy for DMD that works by pre-mRNA splice modulation to restore dystrophin protein production. This approach is

[1]Department of Medical Genetics, Faculty of Medicine and Dentistry, University of Alberta, Edmonton, AB T6G 2H7, Canada. [2]Department of Medicine, Faculty of Medicine and Dentistry, University of Alberta, Edmonton, AB T6G 2G3, Canada. [3]Center for Cardiovascular Research, Division of Cardiology, Department of Medicine, Washington University in St. Louis, St. Louis, MO 63110, USA. [4]Sorbonne Université, Inserm, Institut de Myologie, Centre de Recherche en Myologie, F-75013 Paris, France. [5]Department of Neurology, David Geffen School of Medicine, University of California, Los Angeles, CA, USA. [6]Department of Biomedical Sciences, Carlson College of Veterinary Medicine, Oregon State University, Corvallis, OR 97331, USA. [7]Mazankowski Alberta Heart Institute, University of Alberta, Edmonton, AB T6G 2B7, Canada. [8]The Friends of Garrett Cumming Research & Muscular Dystrophy Canada HM Toupin Neurological Science Research Chair, Edmonton, AB T6G 2H7, Canada. ✉e-mail: toshifum@ualberta.ca

particularly relevant for individuals with deletion mutations in the *DMD* gene which constitutes about 60–70% of the cases[1]. The resulting out-of-frame product from such deletions can, however, be reverted in-frame by skipping certain exons. This leads to the production of a truncated but partially functional dystrophin protein leading to a milder form of dystrophy called Becker muscular dystrophy (BMD)[6]. Presently, four phosphorodiamidate morpholino oligomers (PMOs) have secured FDA approval based on this principle: eteplirsen (Sarepta, targeting exon 51)[7], golodirsen (Sarepta, targeting exon 53)[8], viltolarsen (NS Pharma, targeting exon 53)[9], and casimersen (Sarepta, targeting exon 45)[10]. These PMO therapies are designed to target specific exons, catering to patient cohorts amenable to the respective exon-skipping strategy. However, a considerable portion of DMD patients remain vulnerable due to a lack of applicable therapies. Notably, individuals amenable to exon 44 skipping which constitute about 7% of all DMD patients[11]. These patients, despite presenting with a phenotype less severe than *DMD* exon 51 or 53 skip amenable cohort, experience early loss of ambulation, typically by 11 years of age, with ambulant patients demonstrating significant performance deterioration over time[12–14]. Recently approved micro-dystrophin therapy (Elevidys, Sarepta)[15] can be applicable to these patients but the safety concerns associated with adeno-associated virus (AAV)-mediated delivery may restrict its applicability for older patients with advanced dystrophic conditions[16]. Currently, there are two ongoing clinical trials that focus on skipping exon 44: NS-089/NCNP-02 (NS Pharma, NCT05996003) and AOC 1044 (Avidity Biosciences, NCT05670730). NS-089/NCNP-02 is a dual targeting PMO that has been shown to restore 10.27% dystrophin at 40 mg/kg dosage[17] while AOC 1044, a monoclonal antibody-conjugated PMO, could induce 1.5% exon skipping after a single 10 mg injection[18]. Assessment of their efficacy was, however, limited to skeletal muscles with no report made on their cardiac efficacy. These outcomes necessitate the development of a *DMD* exon 44 skipping therapy with a specific focus on its cardiac manifestations.

A major concern with the currently approved exon-skipping therapies is their limited efficiency. While PMOs are considered to be safe and have greater resistance to degradation, their non-ionic nature impedes their ability to get inside the cells efficiently or escape from endosomes upon entry[19,20]. This holds especially true for cardiomyocytes where clinical trials on the 4 approved PMOs have shown very limited improvements in cardiac conditions[21]. To mitigate such limitations, multiple alternative strategies are being explored among which conjugating cell-penetrating peptides (CPPs) to the PMO has proven to be particularly promising[19]. Previous works from our group have reported a novel CPP called DG9 derived from the protein transduction domain (PTD) of the human polyhomeotic 1 homolog (Hph-1) transcription factor that could significantly increase the PMO delivery to organs that were otherwise unreachable[22–24]. Upon conjugation to DG9, PMO-mediated protein restoration had shown a 4.5-fold increase in the heart[22] and a 5-fold increase in the nerve tissues[23]. However, the underlying mechanism of this enhanced delivery remained unknown.

In this study, we identified a highly effective PMO sequence that can induce *DMD* exon 44 skipping and conjugated it to DG9 to study the mechanism of cellular trafficking in myocytes. Then, we tested the efficiency of this peptide-conjugated PMO (PPMO) in a humanized dystrophic mouse model (h*DMD*del45;*mdx*) which has a human *DMD* transgene integrated into chromosome 5 with an out-of-frame deletion of exon 45[25]. Additionally, this model has the *mdx* point mutation in the murine *Dmd* gene making them unable to produce any human or mouse dystrophin protein[26]. We conducted an extensive pipeline of studies to demonstrate that systemic injection of DG9-PMO can restore a significant amount of dystrophin in both skeletal and cardiac muscles and provide protection against stress-induced cardiac damage. The safety profile of our treatment coupled with normalizing

effects on the transcriptional alternations associated with DMD progression identifies it as a potential therapeutic candidate for patients amenable to exon 44 skipping.

Results

DG9-PMO facilitates enhanced cellular uptake and efficacious nuclear localization

We investigated DG9-PMO's ability to enhance cellular uptake and facilitate effective nuclear localization, crucial steps for the success of exon-skipping therapy in cellular models, in DMD patient-derived immortalized myoblasts and myotubes with exon 45 deletion (del45) as well as cardiomyocytes with no *DMD* mutation. To visualize the cellular uptake of DG9[22,23], we conjugated the peptide to 3'-carboxy-fluorescein-labeled Ac2 PMO at the 5' end. The PMO sequence named Ac2 for exon 44 skipping was employed based on the comparison of 8 different sequences from our previous study that can potentially induce *DMD* exon 44 skipping[27] (Table S1) and their efficacy as determined by the Western blot analysis (Supplementary Fig. 1). Additionally, we verified that conjugation with DG9 produces significantly better results compared to co-transfection (Supplementary Fig. 2a), and that carboxyfluorescein conjugation does not impact the efficiency of DG9-PMO in myotubes (Supplementary Fig. 2b).

Del45 myoblasts, myotubes, and healthy cardiomyocytes were transfected with either 1 μM PMO, 20 μM PMO, or 1 μM DG9-PMO. Intracellular distribution as analyzed by fluorescence microscopy revealed that PMOs were unable to enter the cells even at 20 μM concentration (Supplementary Fig. 3). DG9-PMO, on the other hand, showed a significant PMO internalization at 1 μM concentration (Fig. 1a, Supplementary Fig. 3). Interestingly, DG9-PMO had different intracellular distribution depending on the cell type. In myoblasts, the distribution of DG9-PMO was confined to the cytoplasm, appearing in a punctate pattern around the nuclei, suggestive of association with endocytic vesicles (Supplementary Fig. 4). This distribution was also seen in myotubes and cardiomyocytes, but in these terminally differentiated cells, a substantial amount of DG9-PMO was observed to be localized within the nuclei (Supplementary Fig. 3b). This observation was further confirmed by fractionation studies, where the amount of DG9-PMO in the nuclei of myoblasts was notably low despite having the highest amount of uptake (Fig. 1b). The fractionation process was validated through western blot analysis at 2 h and 24 h time points (Supplementary Fig. 5a). In contrast, nuclear localization in myotubes and cardiomyocytes was much higher, with over 20% of DG9-PMO found in the nuclei at the 12 h mark. Furthermore, a sharp decline in intracellular DG9-PMO concentration was noted in skeletal muscle cells following its removal, unlike in cardiomyocytes, where DG9-PMO was retained, suggesting a more stable intracellular presence in these cells.

The enhanced uptake of DG9-PMO prompted us to identify the mode of endocytosis involved in the trafficking of this PPMO. We used a range of well-studied pharmacological inhibitors for energy-dependent endocytosis inhibition by depleting ATP as well as inhibitors of major endocytic pathways, such as clathrin- and caveolae-mediated endocytosis, and macropinocytosis, at their highest non-toxic concentrations[28]. Following validation of the inhibitors' activity (Supplementary Fig. 5b), we incubated the cells with PPMO in presence of these inhibitors. After 4 h of incubation, uptake was significantly reduced in all groups suggesting DG9-PMO utilizes multiple endocytic pathways to enter the cells (Fig. 1c). While the percentage of endocytosis through a particular pathway differed among cell types, the inhibition caused by EIPA was most significant in myoblasts. This observation suggests that macropinocytosis is the dominant endocytic route in differentiating cells. Conversely, in terminally differentiated cells such as myotubes and cardiomyocytes, no specific preference was noted. Instead, the inhibition of any single pathway resulted in a uniform reduction in PPMO uptake. At the highest non-toxic dosage,
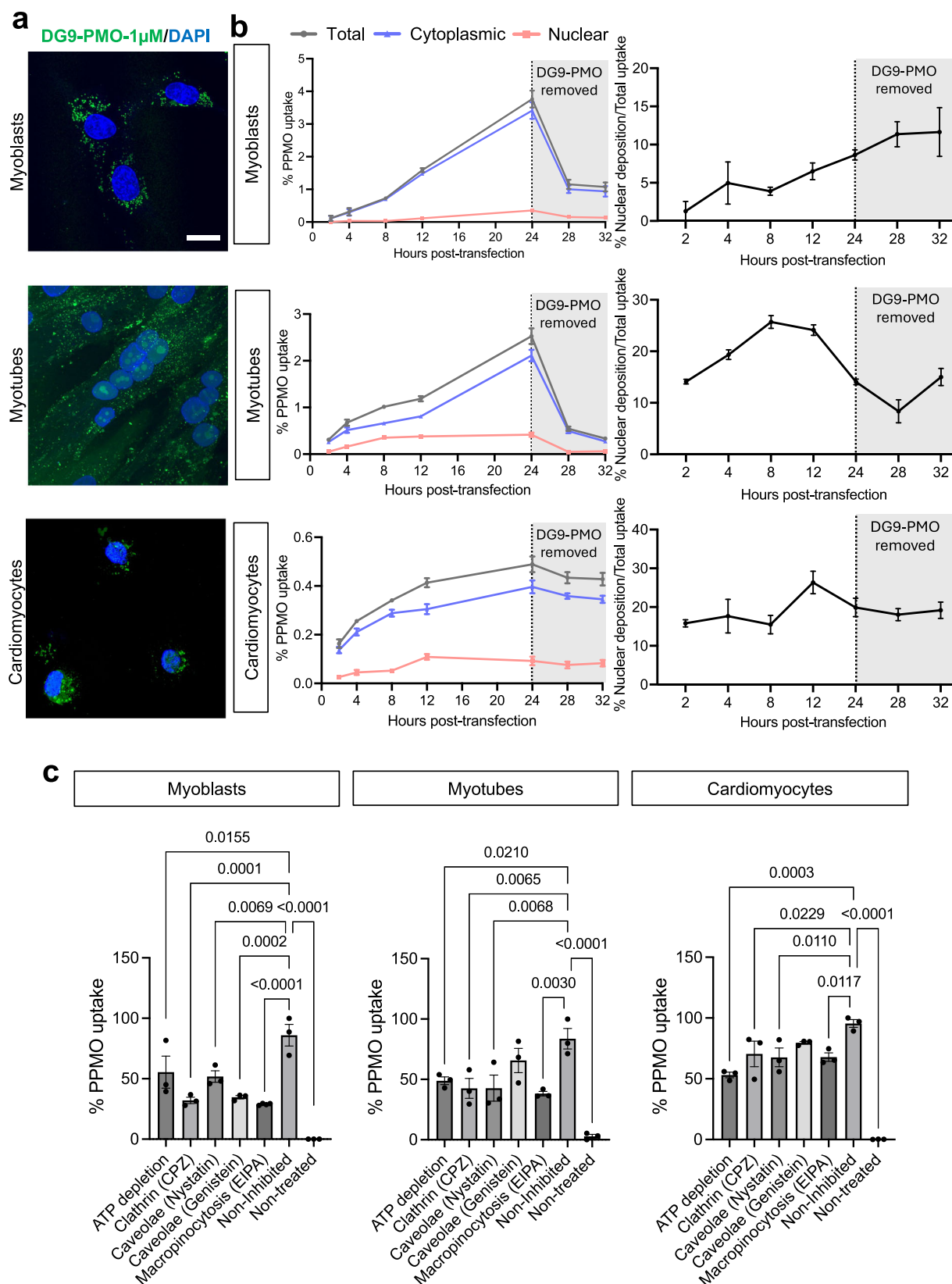
genistein did not have any effects on the PPMO uptake in myotubes or cardiomyocytes. Taken together, these in vitro data suggest that DG9-PMO utilizes multiple energy-dependent endocytic pathways to enter skeletal and cardiac muscle cells which likely results in the increased cellular uptake illustrated in Fig. 1a.

Systemic DG9-PMO administration improves skeletal muscle phenotype in a humanized dystrophic mouse model

To assess the in vivo therapeutic efficacy of DG9-PMO, we performed weekly retro-orbital injections of either saline, 30 mg/kg of DG9-PMO, or 30 mg/kg of PMO once/week for 4 weeks in h*DMD*del45;*mdx* mice[25].

Fig. 1 | Cellular internalization of PMOs after DG9 conjugation. a Representative immunofluorescence images of del45 myoblasts, myotubes, and healthy cardiomyocytes after incubating with 3′-carboxyfluorescein-labeled DG9-PMO at 1 μM (green) for 24 h. Cell nuclei were labeled with DAPI. Scale 20 μm. **b** Time course of the uptake and nuclear localization of DG9-PMO (1 μM) in del45 myoblasts, myotubes, and healthy cardiomyocytes. The shaded region indicates the variations in intracellular DG9-PMO levels following its removal ($n = 3$). **c** Intracellular trafficking of DG9-PMO in del45 myoblasts, myotubes, and healthy cardiomyocytes in presence of different endocytosis inhibitors; NaN3 and 2′-Deoxy-D-Glucose for ATP-depletion, chlorpromazine (CPZ) for clathrin-mediated endocytosis inhibition, nystatin and genistein for caveolae-mediated endocytosis inhibition, and 5-(N-ethyl-N-isopropyl) amiloride (EIPA) for macropinocytosis inhibition ($n = 3$). Statistical analysis: One-way ANOVA with Dunnet's test against non-inhibited. Not significant, $P > 0.05$ (not shown). Error: SEM. Source data are provided as a Source Data file.

As muscle degeneration becomes apparent around the age of 4 weeks in *mdx* mice[29], we decided to initiate our treatment on 8 week-old mice to determine its therapeutic effects. We performed functional assessments at baseline and after the treatments followed by tissue collection after 2 weeks (Fig. 2a). h*DMD*del45;*mdx* mice receiving the DG9-PMO treatment demonstrated significant improvement in both the forelimb and total grip strength tests compared to non-treated (NT) and PMO-treated groups (Fig. 2b). While this improvement in total grip strength was significantly lower than wild-type (WT) controls, the DG9-treated group had a forelimb grip strength comparable to the WT level. Endurance and motor coordination as assessed by treadmill and rotarod tests showed DG9-PMO treated mice could run for an extended period of time with an average improvement of 13% and 31.5%, respectively. This is in contrast to the NT and PMO-treated groups where the NT group had a 34% and 13.4% decline and the PMO-treated group had an 8.2% and 20.9% decline from baseline in the treadmill and rotarod tests, respectively. The functional improvements complemented the results from molecular analyses where DG9-PMO induced over 10% (range 10.9–12.3%) exon 44 skipping efficiency and restored over 16% (range 16.8-21.2%) of WT dystrophin levels in various skeletal muscles (Fig. 2c, Supplementary Fig. 6). On the other hand, the NT group showed 0.8–3.5% of spontaneous exon 44 skipping, expressing about 1.7–3.0% of WT dystrophin. The unconjugated PMO treatment group, having a skipping efficiency of 1.0–5.4% and dystrophin restoration ranging between 1.5–6.7%, did not show any significant improvement over the NT group. Immunofluorescent staining of dystrophin further confirmed the widespread dystrophin restoration showing about 24.6% of dystrophin-positive fibers in the DG9-treated group (Fig. 2d).

Next, we performed histological analyses of skeletal muscles (Supplementary Fig. 7) where the diaphragm showed a significant decrease in the percentage of centrally nucleated fibers (CNFs) in both the DG9-conjugated and unconjugated PMO treatment groups (Supplementary Fig. 7b). No such changes were observed for other skeletal muscles such as tibialis anterior (TA) or quadriceps. From minimum Feret's diameter analysis, we observed an increased number of larger fibers (45-50 μm) in the TA while a higher percentage of smaller fibers (20−25 μm) was present in the quadriceps. This is in contrast to the NT and PMO-treated groups where most fiber sizes ranged between 25–30 and 35–40 μm, respectively for both TA and quadriceps. Diaphragm did not show such changes with most fibers ranging around 12−14 μm for all the treatment groups.

DG9-PMO treatment restores dystrophin production and provides cardio-protection against β-isoproterenol in the heart

One of the primary goals of this study was to develop a therapy for DMD that is effective in the heart—a limitation the currently approved therapies fail to address. While the *mdx* mouse model displays a skeletal muscle phenotype early on, the development of DMD-mediated cardiomyopathy is markedly delayed, typically not manifesting until a much later age[30]. To recapitulate the human cardiac pathology in younger mice, adrenergic agonists such as β-isoproterenol and dobutamine are extensively utilized. These agents increase heart rate and cardiac contractility, inducing damage in susceptible cardiomyocytes and thereby mimicking the stress conditions seen in DMD-related cardi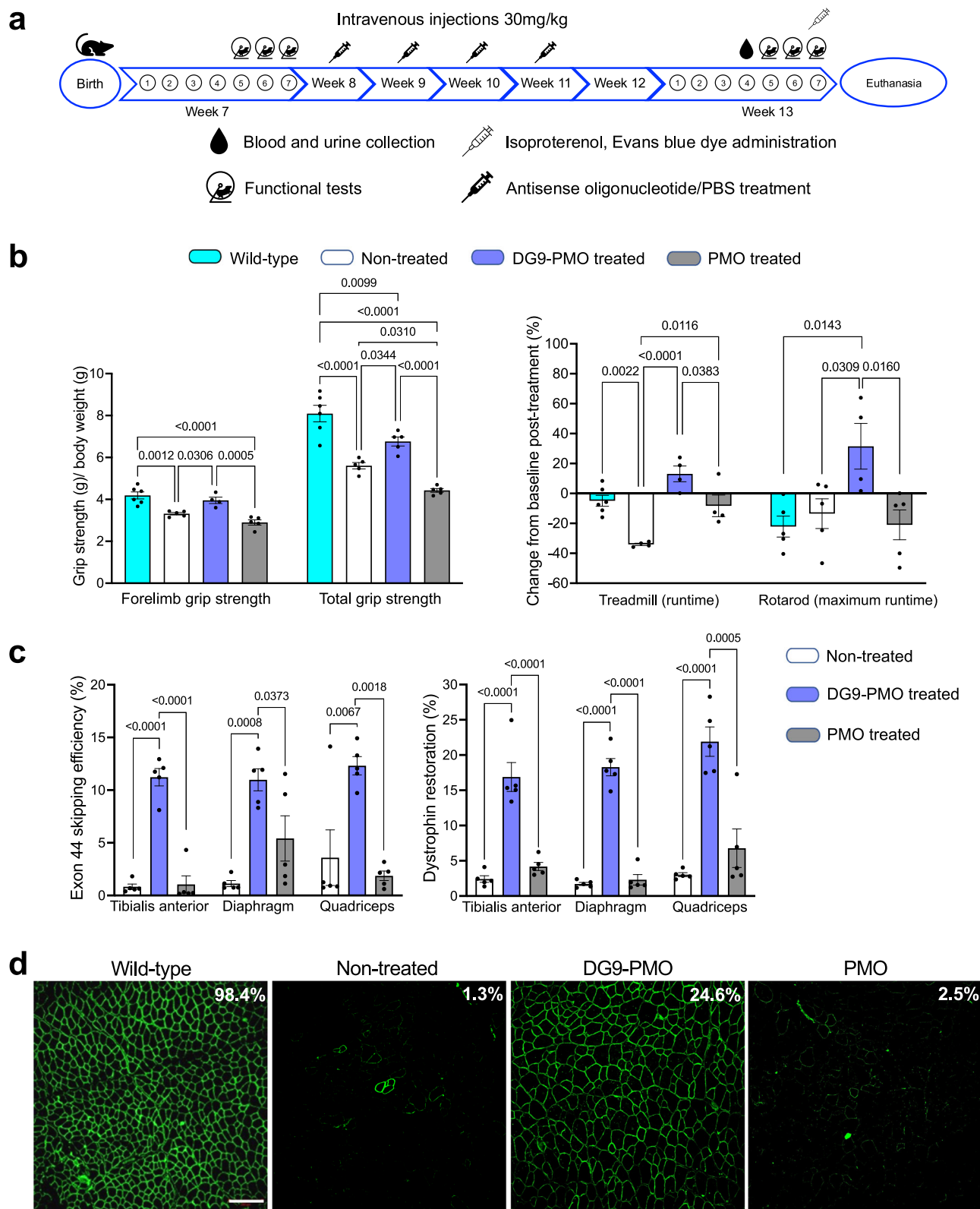ac dysfunction[31–34]. To evaluate the effects of DG9-PMO in the heart, we performed a single subcutaneous injection of 15 mg/kg β-isoproterenol to cause cardiac damage along with an intraperitoneal injection of Evans blue (EB) dye to detect cardiomyocyte degeneration 24 h before euthanasia (Fig. 2a). Molecular analysis of cardiac tissues revealed DG9-PMO to be highly effective inducing over 20% exon 44 skipping whereas the NT and PMO-treated groups showed 1.6% and 4.2% skipping, respectively (Fig. 3a). At the protein level, DG9-PMO was able to restore over 41% dystrophin in the heart significantly outperforming the NT (4.5%) and the PMO treatment (4%) groups. Widespread dystrophin restoration was further confirmed by the presence of 43.4% dystrophin-positive fibers while the NT and PMO-treated groups had <1% (Fig. 3b).

The impact of β-isoproterenol-induced cardiac damage was clearly observed in our mouse model, with the NT group displaying ~18% cardiomyocyte degeneration, as estimated from the EB-positive area shown in Fig. 3b. The unconjugated PMO treatment group had a similar amount of EB dye uptake which was around 16.7%. In contrast, DG9-PMO-treated mice had a significant reduction in cardiomyocyte degeneration (2.4%) such that they were not statistically different from the WT group (0.6%). Further examination revealed an increase in collagen deposition in the saline-treated group (120.3%) when compared to the WT group (87.9%), as demonstrated by the collagen-to-laminin ratio. The DG9-conjugated PMO treatment group showed a decrease in collagen deposition to 103.3%, which, while improved, did not reach statistical significance compared to the WT or unconjugated PMO (111.3%) treatment groups, as shown in Supplementary Fig. 8.

To evaluate functional changes in the heart, we administered subcutaneous injections of isoproterenol at a dose of 1.5 mg/kg every day for 2 weeks to 10 week-old h*DMD*del45;*mdx* mice. These mice also received two doses of 30 mg/kg DG9-PMO or saline via retro-orbital injection once a week. A wild-type group treated with the same treatment regimen of isoproterenol was used as control. Echocardiographic imaging was performed before and after the treatment (Fig. 3c). The dystrophic group that received only isoproterenol treatment showed a significant decline in heart function, with a 19% reduction in fractional shortening (FS) and a 13.8% decrease in ejection fraction (EF) (Fig. 3d, Supplementary Fig. 9, Table S2). In contrast, the isoproterenol-treated mice receiving DG9-PMO maintained normal cardiac systolic function, showing no statistically significant differences from the WT group (FS: -1.6% DG9-PMO, 2.3% WT; EF: 0.4% DG9-PMO, 1.9% WT). We also analyzed serum cardiac troponin I levels but could not find significant differences between any of the groups (Fig. 3e).

Normalized liver and kidney injury biomarkers with reduced skeletal muscle inflammation post-DG9-PMO treatment

To evaluate the safety of our cell penetrating peptide, we performed tail-vein blood sampling 10 days after the last injection followed by serum analysis for biomarkers such as aspartate aminotransferase (AST), alanine transaminase (ALT), creatine kinase (CK), blood urea nitrogen (BUN), gamma-glutamyl transferase (GGT), and creatinine (Fig. 4a). The NT and PMO-treatment groups had significantly elevated AST and ALT levels; however, the DG9-PMO treatment normalized their levels to such an extent where there was no statistical difference with the WT group (mean: AST, 63.8 U/L WT, 66.5 U/L DG9; ALT, 30.8 U/L WT, 28 U/L DG9). The considerably elevated concentration of

a Intravenous injections 30mg/kg

Birth — Week 7 ① ② ③ ④ ⑤ ⑥ ⑦ — Week 8 — Week 9 — Week 10 — Week 11 — Week 12 — Week 13 ① ② ③ ④ ⑤ ⑥ ⑦ — Euthanasia

Blood and urine collection | Isoproterenol, Evans blue dye administration
Functional tests | Antisense oligonucleotide/PBS treatment

b Wild-type | Non-treated | DG9-PMO treated | PMO treated

c Non-treated | DG9-PMO treated | PMO treated

d Wild-type 98.4% | Non-treated 1.3% | DG9-PMO 24.6% | PMO 2.5%

skeletal muscle damage biomarker, CK, in the NT group (3813 U/L) was reduced to the normal level (320 U/L WT) after DG9-PMO treatment (646.2 U/L). Mice in the PMO-treatment group also had a significant reduction in the CK level (1493.5 U/L). Interestingly, The BUN level—an indicator of kidney dysfunction—was increased in the DG9-PMO treated group (32.25 mg/dL) compared to the NT group (25.6 mg/dL). This change, however, was not statistically different from the WT (28.4 mg/

dL, $P = 0.1557$) or the PMO-only (29.8 mg/dL, $P = 0.5015$) groups. To confirm the effects of DG9-PMO on the kidney, we performed urinary kidney injury molecule 1 (KIM-1) analysis which is a more sensitive marker for renal injury[35]. Here, we found no significant difference between any treatment groups suggesting no apparent toxic effects of DG9-PMO on the kidney. Qualitative histological analysis of the liver and kidney showed no signs of cell degeneration serving as further

Fig. 2 | Skeletal muscle improvement after DG9-PMO treatment. a Eight week-old male h*DMD*del45;*mdx* mice were treated retro-orbitally four times once/week with either saline, DG9-PMO, or PMO at 30 mg/kg bw. Saline-treated WT served as control. Functional tests were conducted before and 1 week after treatment. Blood and urine samples were collected 10 days post-treatment. Tissues were collected 2 weeks after the last injection. All mice received a 15 mg/kg subcutaneous injection of β-isoproterenol and 1% Evans blue dye intraperitoneally 24 h before sacrifice. **b** Forelimb and total grip strength of individual groups of mice normalized to their body weight after treatment. Changes in endurance and coordination compared to baseline measured using treadmill and rotarod (*n* = 4–6). **c** Quantification of exon 44 skipping by RT-PCR (left) and dystrophin restoration by western blot (right) in various skeletal muscles after treatment (*n* = 5). Dystrophin (Leica, NCL-DYS1) restoration presented relative to wild-type control after normalization with desmin (Abcam, ab8592). Statistical analysis: One-way ANOVA with Tukey's test. Not significant, *P* > 0.05 (not shown). Error: SEM (**b**, **c**). **d** Representative immuno-fluorescence images for dystrophin (ab15277) in TA muscles. Percentage of dystrophin-positive fibers calculated in relation to laminin. Scale 200 μm. Source data are provided as a Source Data file.

evidence of the treatment's safety (Supplementary Fig. 10a). Changes in serum GGT and creatinine could not be analyzed as their concentrations were below the detection level (Supplementary Fig. 10b). Body weights did not significantly differ between any of the groups post-treatment where the average weight gain was 5.4–10.7% for all the mice after the 6 weeks study period (Supplementary Fig. 10c). We did, however, observe a trend where NT and PMO-treated mice gained more weight and DG9-PMO treated mice gained less weight than WT over the course of the study.

As dystrophic muscles continuously undergo myonecrosis and cause inflammation, we decided to look into the presence of inflammatory cells in skeletal muscles. We stained the tibialis anterior muscles with CD68 antibody—a marker expressed by cells in the monocyte lineage (Fig. 4b). Quantification of CD68$^+$ cells in the NT and PMO-treated groups showed a significantly higher number of CD68$^+$ cells compared to WT. In contrast, the DG9-treated mice had a reduced number of CD68$^+$ cells which was statistically indifferent from the WT group suggesting amelioration of muscle inflammation.

DG9-PMO alters gene expression in skeletal and cardiac muscles towards normalization

To assess the global impact of DG9-PMO on gene expression, we conducted bulk RNA sequencing on WT, NT, and DG9-PMO-treated mice, with a focus on 13 week-old animals (Fig. 5, Supplementary Fig. 11). Our analysis revealed 4537 differentially expressed genes (DEGs) in the TA muscle of dystrophic mice compared to WT controls, while treatment with DG9-PMO resulted in 510 DEGs relative to the untreated group (Fig. 5a). However, when compared to the healthy WT group, the DG9-PMO-treated mice exhibited 430 DEGs, comprising 68 upregulated and 14 downregulated genes beyond a log$_2$-fold change of 2 and -2, respectively (Supplementary Fig. 11a). Of these 430 DEGs, 373 genes overlapped with the dystrophic group with a consistent change in expression suggesting these changes were caused by the dystrophic condition rather than the treatment. Importantly, our analysis revealed a clear contrast in the expression profile of these genes in the DG9-PMO treatment group, highlighting its potential to restore aberrant gene expression, as demonstrated in the comparison between treated and dystrophic mice. Analysis of the heart samples showed 3664 DEGs in the NT dystrophic mice with the healthy control as reference while the treatment induced a significant change in 908 genes (Fig. 5a). These changes in gene expression caused by the treatment were such that the treated group had only 4 genes with different expression from the WT group (Supplementary Fig. 11b).
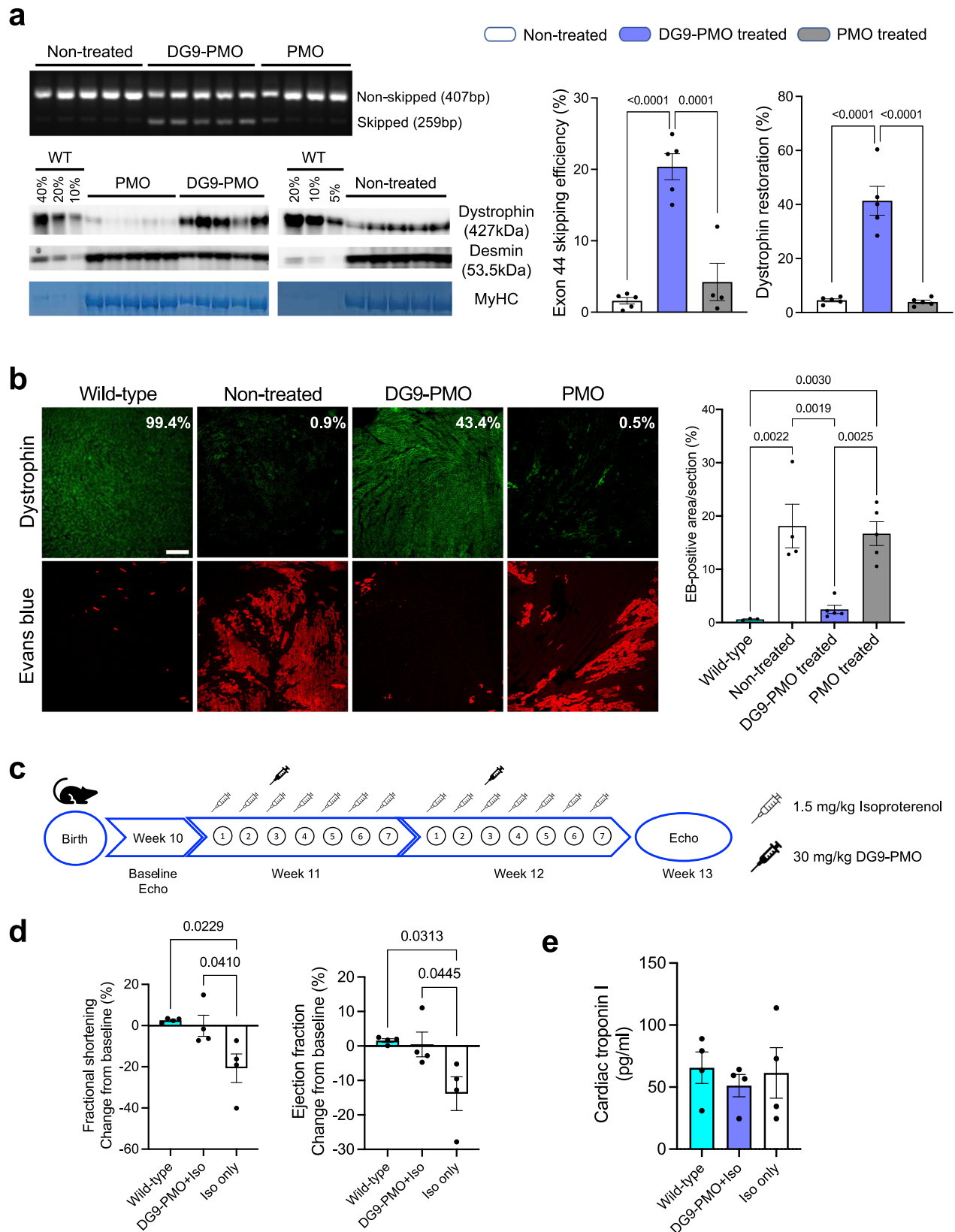
To evaluate the relevance of our therapy in human patients, we compared our RNAseq dataset to the gene signatures of DMD patients (Fig. 5b). Bulk RNA sequencing of patient TA biopsy samples by Nieves-Rodriguez et al.[36] showed 868 DEGs where 318 genes overlapped with our NT dystrophic group. Regression analysis of these genes showed a weak correlation (R^2 = 0.23)—a likely outcome reflecting the difference in species, mutation in the *DMD* gene, and stages of pathogenesis. Despite this weak correlation, 85% of these genes shared the same directional shift in gene expression indicating the suitability of our humanized mouse model for DMD-related studies. Similarly, we compared the DEGs in dystrophic mouse hearts with the iPSC-derived cardiomyocyte dataset from Kamdar et al.[37]. Out of the 864 DEGs

found in human cardiomyocytes, we identified 425 genes overlapping with our dataset. Gene alterations in humans and mice had a higher correlation (R^2 = 0.35) than that of TA with over 95% of genes exhibiting the same directional shift. Next, we analyzed the expression changes of these overlapping DEGs to determine the effects of our DG9-PMO treatment. Heatmaps showing the 50 most significantly altered genes in the dystrophic mice that are also differentially expressed in DMD patients had an opposite expression pattern after treatment (Fig. 5c). While this normalizing effect was not significant for all the genes (treated vs dystrophic), the resulting shift in expression showed the treated mice had a profile where most gene expressions were statistically indifferent from the WT group. Moreover, this normalizing pattern held true for the genes that were differently expressed in humans and mice observed in Fig. 5b (Supplementary Fig. 11c).

While the treatment exhibited an overall restorative effect on aberrantly expressed genes caused by the dystrophic condition, we were also interested in the 510 and 908 DEGs that resulted from the treatment in the dystrophic mice in the TA and heart, respectively (Fig. 5a). Interestingly, all the DEGs post-treatment had an opposite expression profile in the dystrophic vs WT group further supporting the notion of the normalizing effects of DG9-PMO (Supplementary Data 1). Next, we performed the Gene ontology (GO) analysis for these significantly altered genes in the treated group in reference to the NT to identify the processes affected by our therapy using Metascape[38] (Supplementary Data 2). In the TA, genes associated with organ and system development pathways were upregulated while the downregulated genes were mostly related to cell growth and apoptosis (Fig. 5d). Heart, on the other hand, showed upregulation in genes responsible for functional processes such as cardiac conduction, muscle contraction, and calcium homeostasis with downregulation of genes associated with inflammation and apoptosis. Taken together, these data strongly suggest that DG9-PMO treatment mitigates the abnormal gene expression in the dystrophic muscles by inhibiting genes related to cell regeneration and inflammation and accelerating processes such as structural development, functional restoration, and synapse formation.

DG9-PMO is significantly more effective than R6G-PMO in the heart

Finally, we compared the efficacy of our peptide with the benchmark peptide R6G which was under clinical trial until very recently (NCT04004065)[39]. We conjugated the DG9 and R6G peptide to the 3' end of the Ac2 PMO. h*DMD*del45;*mdx* mice were injected 2 times once/week at 30 mg/kg of either DG9-PMO (equivalent to 2190 nmol/kg) or R6G-PMO (equivalent to 2689 nmol/kg) (Fig. 6a). Tissue samples were collected after 1 week. Western blot analysis showed no notable difference in dystrophin production within the tibialis anterior (TA) muscle between the two peptide-conjugated PMOs (DG9 1.9%, R6G 3.5%) (Fig. 6b). However, in the heart, dystrophin protein levels were significantly higher after treatment with DG9-PMO (5.3%) compared to R6G-PMO (1.8%). This result was also reflected in the RT-PCR analysis, where exon skipping efficiency in the TA was 16.45% for DG9-PMO and 20.21% for R6G-PMO, with no statistically significant difference (Fig. 6c). In contrast, the heart showed a significantly higher exon skipping efficiency (17.08%) in the DG9-treated group compared to the R6G group (5.5%). Immunofluorescence staining further confirmed

despite the recent advances in their chemistry[19]. Even though PMOs are third-generation ASOs with enhanced safety and efficacy, their clinical utility remains hampered by issues such as poor cellular uptake, rapid clearance from circulation, and their inability to escape from endosomes[19]. To circumvent such issues, we have conjugated the PMO to our recently developed CPP called DG9[22,23] which has

these findings, demonstrating the presence of dystrophin-positive fibers across different treatment groups (Fig. 6d).

Discussion
Our study addresses the critical challenge of effective delivery of therapeutic agents, particularly ASOs, which have multiple limitations

Fig. 3 | DG9-PMO provides cardio-protection after β-isoproterenol induced cardiac damage by restoring dystrophin production. a RT-PCR of exon 44 skipping and western blot (NCL-Dys1) results post-treatment in the heart. Proteins were loaded at 40 μg for NT and treated along with indicated percentages for the WT. Desmin (ab8592) and MyHC serve as loading controls. Quantification is shown on the right relative to wild-type control after normalization with desmin (n = 4–5). **b** Representative immunofluorescence images for dystrophin (green, ab15277) in the heart. Percentage of dystrophin-positive fibers calculated in relation to laminin. Evans blue dye uptake as a result of β-isoproterenol induced cardiac damage shown in red. Quantification is shown on the right (n = 3–5). **c** 10 week-old

male h*DMD*del45;*mdx* mice were treated with 1.5 mg/kg of β-isoproterenol (subcutaneous) every day for 14 days. These mice also received two 30 mg/kg doses of DG9-PMO or saline once/week retro-orbitally. Isoproterenol-treated WT served as control. Echocardiogram tests were conducted before and 1 day after treatment. Blood samples were collected after the treatment. **d** Changes in fractional shortening and ejection fraction compared to baseline after 2 weeks of isoproterenol treatment (n = 4). **e** Levels of cardiac troponin I in serum after isoproterenol and DG9-PMO injection (n = 4). Statistical analysis: One-way ANOVA with Tukey's test. Not significant, P > 0.05 (not shown). Error: SEM. Scale 200 μm. Source data are provided as a Source Data file.
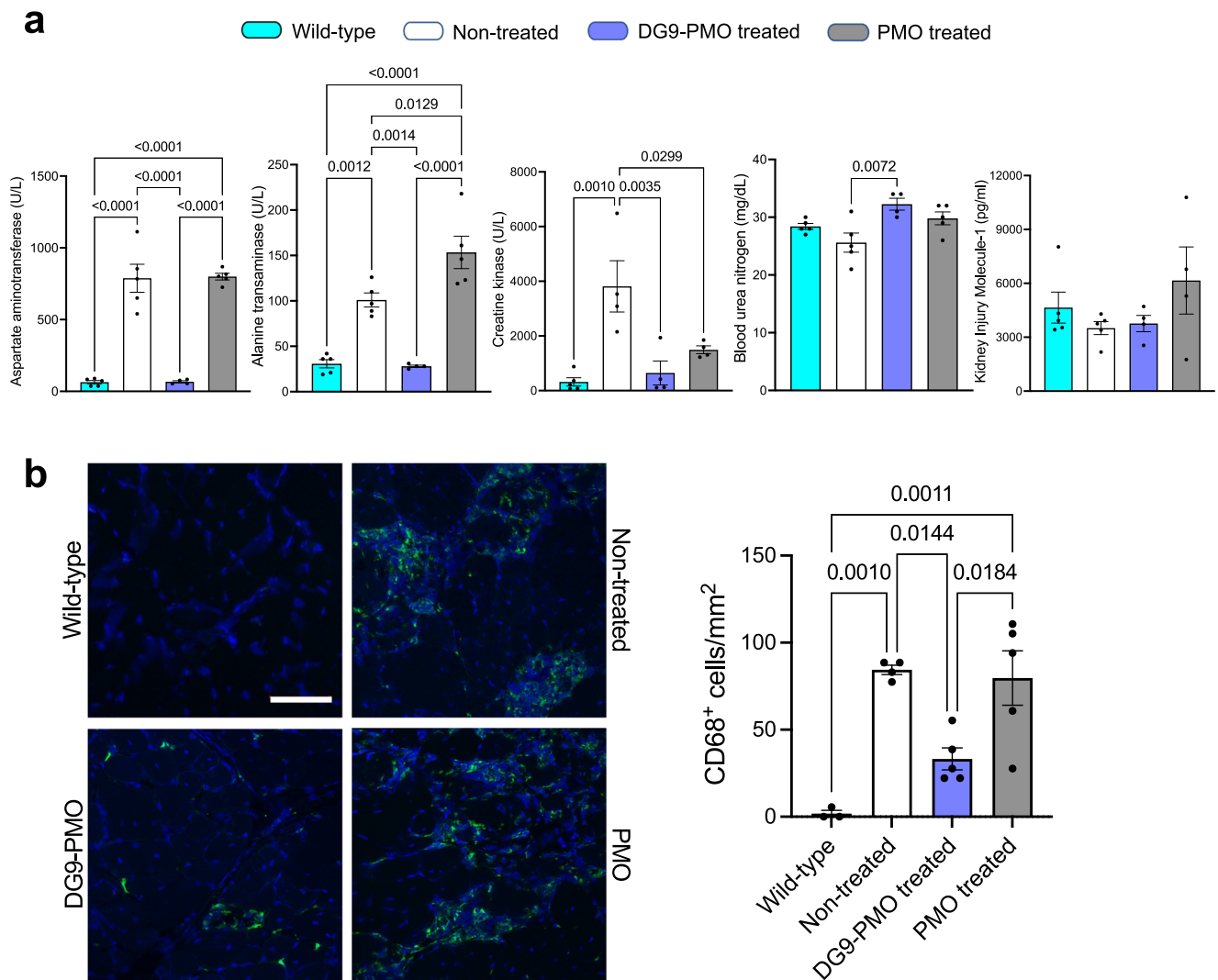

Fig. 4 | Normalized liver and kidney biomarker levels with reduced inflammation in skeletal muscles post-treatment. a Analysis of different liver-specific (aspartate aminotransferase, alanine transaminase, creatine kinase) and kidney-specific (blood urea nitrogen) biomarkers from serum samples collected 10 days post-treatment. Kidney injury molecule 1 (KIM-1) was analyzed from urine samples collected at the same time point (n = 4–5). **b** Representative immunofluorescence images for CD68⁺ cells (green, MCA1957T) with DAPI staining. Quantification shown on the right (n = 3–5). Statistical analysis: One-way ANOVA with Tukey's test. Not significant, P > 0.05 (not shown). Error: SEM. Scale 100 μm. Source data are provided as a Source Data file.

demonstrated its effectiveness in delivering PMO to various tissues. However, its precise mechanism of cellular entry has remained unclear. By comparing the intracellular localization of fluorescent-tagged PMO and DG9-PMO across different cell types relevant to DMD, we have revealed the distinct cellular distributions of DG9-PMO (Fig. 1a). Notably, DG9-PMO exhibited remarkable uptake across all myocytes, but with varying localization patterns. In myoblasts, DG9-PMO tended to aggregate around the nuclei likely as a result of

endosomal entrapment (Supplementary Fig. 3-4). Myotubes, in contrast, had a diffused distribution of DG9-PMO throughout the cytoplasm with a significant portion localized inside the nuclei (Fig. 1b). Previous studies have speculated the possibility of uneven PPMO uptake in undifferentiated and differentiated cells based on the fact that PPMO is more effective in certain muscles such as the TA over other skeletal muscles[28,40]. This may also be due to different metabolic rates of these cells since myoblasts are actively dividing cells with a

high metabolic rate, whereas myotubes are terminally differentiated cells with most of their activity mainly focused on the contractile apparatus[41,42]. This preferential localization of PPMO within the nuclei in differentiated cells is further evidenced by our cardiomyocyte

results where a strong nuclear accumulation of PPMO can be observed (Fig. 1b). Furthermore, skeletal muscle cells exhibited a rapid decline in intracellular DG9-PMO concentration following its removal, in contrast to cardiomyocytes, where DG9-PMO remained. This retention in
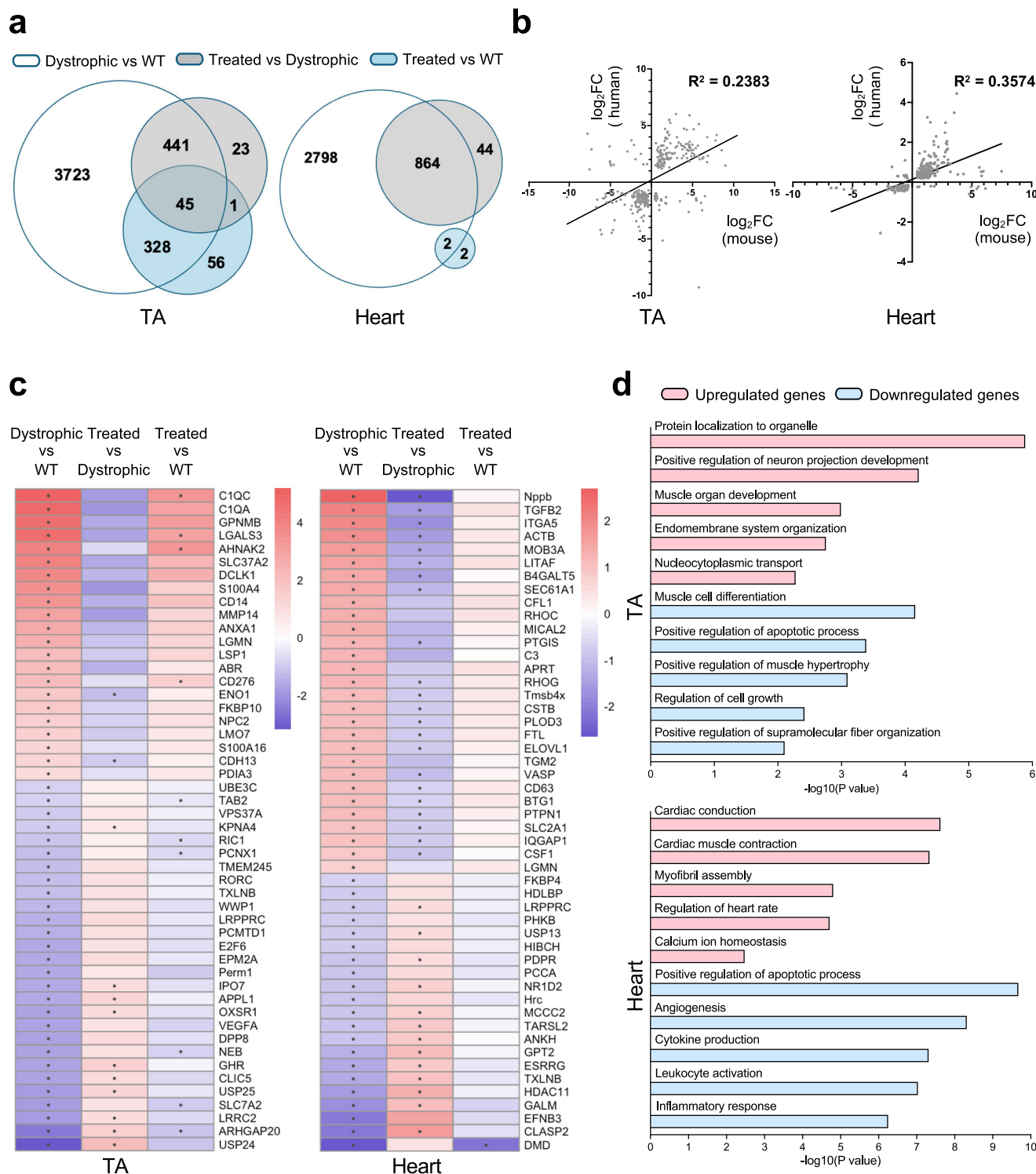
Fig. 5 | RNA sequencing analysis of DG9-PMO therapeutic efficacy. a Venn diagram showing the number of unique and overlapping differentially expressed genes (DEGs) in different treatment groups for the TA and heart; NT compared to WT, DG9-PMO treated compared to NT and WT ($n = 4$). **b** Regression analysis of the log2(fold-change) values of overlapping DEGs in h*DMD*del45;*mdx* mice and DMD patient TA muscles (Nieves-Rodriguez et al.[36]) or iPSC-derived cardiomyocytes (Kamdar et al.[37]). **c** Heatmaps displaying the expression changes in the TA and heart

as a result of the treatment. Top 50 DEGs, common for both humans and mice, with the highest statistical significance in dystrophic mice compared to WT are presented. High expression indicated by red with blue indicating low expression. Dots represent significantly altered gene expression ($P < 0.05$). Statistical analysis: Two-sided Wald test with Benjamini-Hochberg multiple testing correction. **d** Selected top GO terms enriched in up and downregulated genes after DG9-PMO treatment in reference to NT. Analysis was done using Metascape[38].

cardiomyocytes could be attributed to the lower turnover rate of cardiac cells which may have facilitated greater accessibility to DG9-PMO leading to an increased nuclear accumulation. PMO, on the other hand, had negligible cellular internalization even at 20 times the DG9-PMO dosage (Supplementary Fig. 3a, 4). The mechanism of PMO uptake is still ambiguous with some studies attributing the
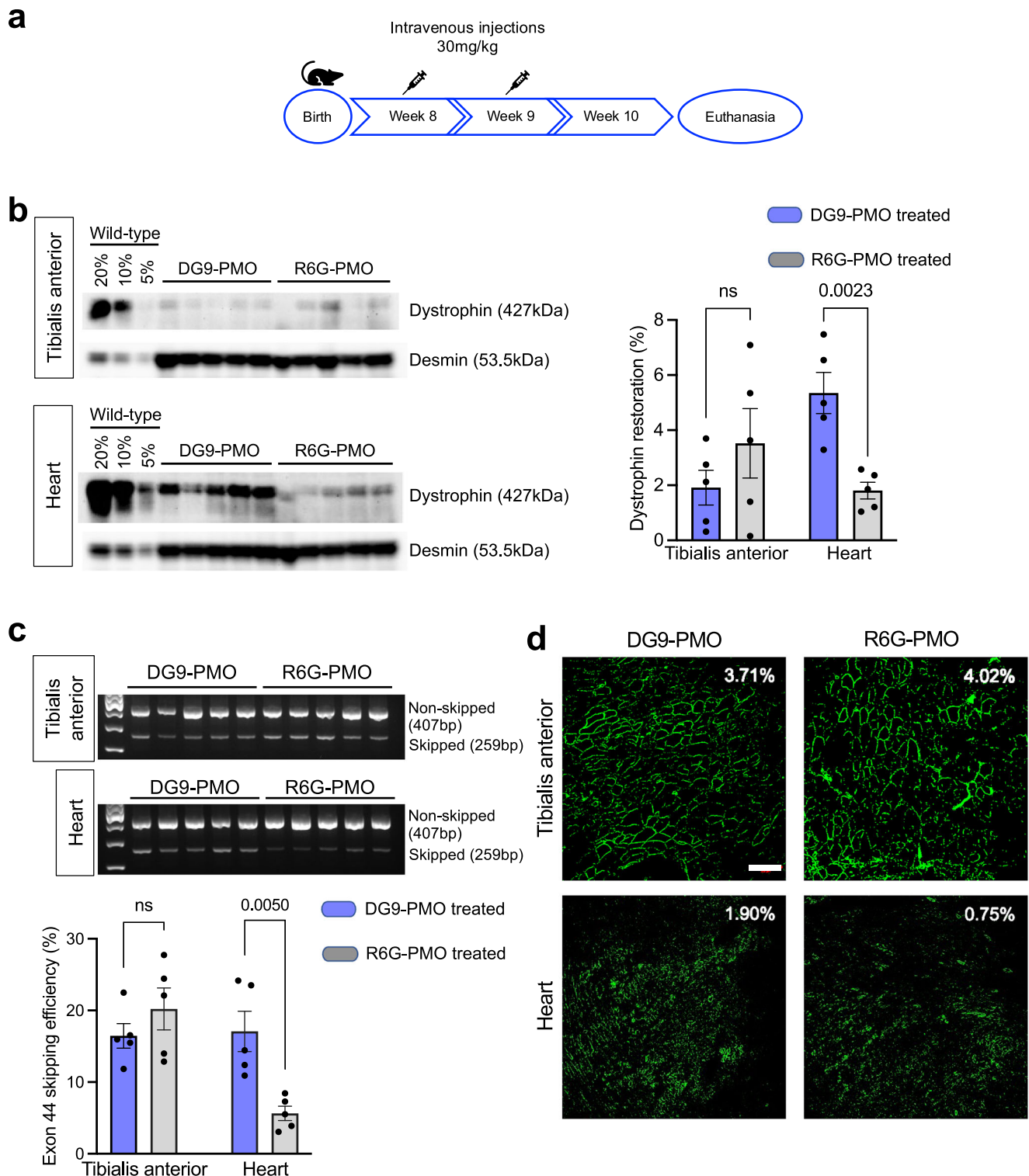

Fig. 6 | Comparison between DG9- and R6G-PMO. a Schematic diagram of the treatment regimen. Eight week-old male h*DMD*del45;*mdx* mice were treated retro-orbitally twice, once/week, with DG9-PMO or R6G-PMO at 30 mg/kg (equivalent to 2190 nmol/kg for DG9-PMO, 2689 nmol/kg for R6G-PMO). Tissues were collected 1 week post-treatment. **b** Western blot (NCL-Dys1) images post-treatment in TA and heart. Proteins were loaded at 40 μg for NT and treated along with indicated percentages for the WT. Desmin (ab8592) serves as loading control. Quantification is shown on the right relative to wild-type control after normalization with desmin (*n* = 5). **c** RT-PCR of exon 44 skipping in TA and the heart. Quantification is shown at the bottom (*n* = 5). **d** Representative immunofluorescence images for dystrophin (ab15277) in TA and heart muscles. Percentage of dystrophin-positive fibers calculated in relation to laminin. Scale 200 μm. Statistical analysis: unpaired two-tailed *t*-test. Error: SEM. Source data are provided as a Source Data file.

internalization to the "leakiness" of the dystrophic membrane[43], some studies suggesting PMO internalization occurs during the process of myogenesis[44] while another study has shown PMO to be endocytosed through a caveolin-dependent pathway[45]. Regardless, in our study, we did not find any significant PMO uptake quite possibly because a higher concentration of PMO was required to have an observable effect. Another less likely reason might be the absence of "leakiness" in the membrane as the cells were not subjected to any sort of physical stress unlike a dystrophic muscle undergoing contraction/relaxation. This distinct internalization pattern of PMO and PPMO underscores the importance of understanding cellular uptake mechanisms to optimize therapeutic strategies for DMD.

The advantage of DG9-PMO over PMO was further demonstrated by their mechanism of cellular entry (Fig. 1c). We used multiple pharmacological reagents at their highest non-toxic dosage to inhibit specific endocytic pathways. Our results demonstrate that DG9-PMO uses multiple energy-dependent pathways to enter the cells. In myoblasts, we observed an inclination to macropinocytosis-mediated entry as EIPA had the most pronounced effect on PPMO uptake. Interestingly, myotubes and cardiomyocytes show no preference for a specific entry pathway, suggesting potential cell-type-specific differences in DG9-PMO uptake mechanisms. This is in contrast to previously reported PPMO (Pip6a-PMO) and PMOs where studies have shown them to be exclusively reliant on a single-entry pathway[28,45] highlighting the versatility of DG9 peptide in delivering cargos in a diverse range of cell types. Furthermore, DG9-PMO's resistance to protease/peptidase-mediated degradation in serum-containing media indicates their enhanced stability and bioavailability, further supporting its candidacy for clinical applications[40].

A major goal of this study was to develop an exon 44 skipping therapy for DMD patients, with a particular emphasis on addressing its cardiac complications. Through in vitro analysis, we identified a PMO sequence (Ac2) capable of inducing nearly 100% exon 44 skipping and over 80% dystrophin protein expression (Supplementary Fig. 1). Subsequent evaluation in hDMDdel45;mdx mice revealed that conjugation of the PMO with the DG9 peptide significantly improved muscle function and motor coordination after a four-week treatment regimen (Fig. 2). The DG9-PMO, on average, showed a 4-fold increase in exon skipping and dystrophin restoration compared to unconjugated PMO in skeletal muscles. In the cardiac muscles, the effects of DG9-PMO were more evident showing a 4.8-fold increase in exon skipping and a 10-fold increase in dystrophin restoration (Fig. 3). Previous studies have demonstrated a discrepancy between the level of exon skipping and subsequent dystrophin restoration[22,46] which did not happen in our case suggesting that the exon 44-45 skipped transcript is more stable than its 51-52 skipped counterpart. In a more recent study, Watanabe et al.[47] developed a PMO (NS-089/NCNP-02) that simultaneously targets two splicing regulators in exon 44 and a 13 week 2000 mg/kg treatment in cynomolgus monkeys induced 9.5% exon 44 skipping in skeletal muscles and about 1.4% skipping in the heart. We observed a similar outcome in our PMO-only treatment group which emphasizes the importance of an efficient delivery system for PMOs in maximizing therapeutic efficacy.

In addition to elucidating the mechanism of cellular entry and determining the efficacy in skeletal and cardiac muscles, we have verified the cardioprotective effects of our therapy—an aspect often overlooked in DMD-related studies. Currently available preclinical models exhibit a late onset of DMD-mediated cardiomyopathy as opposed to its early manifesting skeletal muscle phenotypes, making it difficult to assess the cardiac efficacy of a treatment[48]. To replicate the stress conditions associated with DMD-related cardiac dysfunction, we administered β-isoproterenol to younger mice, employing both a single high-dose and a multiple low-dose treatment regimen to induce cardiac damage. Results from our acute β-isoproterenol injury study demonstrated significantly reduced cardiomyocyte degeneration after

DG9-PMO treatment, which we did not observe in the PMO-treated mice suggesting the limitation of PMO as a long-term therapy for treating DMD-mediated cardiomyopathy (Fig. 3a, b). Further inspection of collagen deposition did not show any significant reduction post-DG9-treatment (Supplementary Fig. 8); however, the downregulation observed in collagen-expressing-genes strongly indicates the treatment would continue to prove beneficial in a weakened heart typically observed in older mice[30] (Supplementary Fig. 11d). Moreover, we observed an upregulation in the MYOC gene and downregulation of the CILP gene which has previously been identified as anti-fibrotic and pro-fibrotic genes, respectively[36] (Supplementary Data 1). These results are consistent with our chronic multiple-dose treatment study, where we observed that DG9-PMO confers cardioprotection against β-isoproterenol. Unlike the NT group, which showed a significant decline in both fractional shortening and left ventricular ejection fraction (LVEF), the DG9-PMO-treated group exhibited no noticeable reduction in either parameter (Fig. 3c, d). No significant changes were observed in cardiac structure or troponin I (cTnI) levels (Table S2, Fig. 3e). Matsumura et al.[49] previously reported that elevated cTnI levels are typically seen in patients during their second decade of life, which may explain the absence of significant changes in cTnI levels and cardiac structure in our study. They also demonstrated that cTnI and LVEF are independent markers, with cTnI reflecting cardiac degeneration and LVEF indicating cardiac stress, while brain natriuretic peptide (BNP), a marker of cardiomyopathy, is strongly associated with LVEF. Consistent with these findings, our acute treatment study revealed a significant reduction in the gene expression of natriuretic peptide B (Nppb; also known as BNP) following DG9-PMO administration (Fig. 5c). The normalization of LVEF and the reduced Nppb expression suggest that DG9-PMO has the potential to mitigate DMD-related cardiac complications effectively.

Safety remains to be the major concern in the development of peptide conjugate PMO therapies. Previously, we discussed the amino acid composition of DG9 peptide where certain L-arginine residues were substituted with D-arginine and the absence of 6-aminohexanoic acid residues making the peptide much safer for clinical use[22,50]. Indeed, our safety and toxicity analysis showed DG9-PMO normalized all serum biomarkers (Fig. 4a) without having any detrimental effects on the liver and kidney (Supplementary Fig. 10). While the changes in body weights were not statistically different in any of the groups, we did observe the reduced weight gain of the DG9-PMO treated mice compared to NT and PMO-only groups. This may be explained by the increased activity post-treatment of the otherwise lethargic mice. The reduction in skeletal muscle tissue inflammation is suggestive of the fact that DG9-PMO reduces myonecrosis (Fig. 4b). RNA sequencing data further supports this notion where processes like cell growth, differentiation, and apoptosis were downregulated (Fig. 5d). Gene expression data demonstrated a strong normalization effect in both TA and heart (Fig. 5c, Supplementary Fig. 11). Treatment effects on the heart were more apparent where genes related to functional improvements exhibited strong upregulation while inflammation-related genes were downregulated. Of the 4 differentially expressed genes found in the treatment group in reference to the WT, DMD continued to be downregulated with a negligible upregulation showing in the treated dystrophic group (Supplementary Fig. 11b). Analysis of the transcript ID cross-matched with the murine Dmd gene suggesting the restored dystrophin product resulted from the integrated human DMD gene without any effects from its murine counterpart. A normalizing effect on the other 3 genes was also observed post-treatment which are mainly associated with processes such as neuron projection development, cytoskeletal formation, and cation channel regulation. These findings collectively underscore the safety and therapeutic potential of DG9-PMO in the treatment of DMD, offering insights into its mechanism of action and broader implications for clinical translation.

In summary, we have developed a peptide-conjugated PMO therapy targeting exon 44 for the treatment of DMD. The treatment demonstrated significant improvements in disease pathology within both skeletal and cardiac muscles. This improved outcome is most likely due to DG9's exploitation of multiple entry pathways, contrasting with the single pathway-mediated entry commonly observed in other PPMOs. Safety assessments revealed no adverse effects associated with the treatment. With its high efficacy and excellent safety profile, we expect this therapy will pave the way for new therapeutic strategies in the field of DMD, warranting further exploration through future clinical trials.

Methods

Cell culture

The immortalized human muscle cells with the deletion of exon 45 (reference no. AB1323DMD14S), henceforth termed del45, were kindly provided by the Institut de Myologie, France. Myoblasts were grown in growth media containing DMEM/F12 medium (with HEPES; Gibco), 20% fetal bovine serum (Sigma), 1 vial of skeletal muscle growth supplement mix (Promocell), and 0.5% Penicillin-Streptomycin (Gibco). Myoblasts were seeded into Nunc™ Cell-Culture Treated 12-well plates (Thermo Scientific) at a density of 1×10^5 cells/well. For myotubes, growth media was replaced by differentiation media once the myoblasts were 90% confluent. Differentiation media was prepared using DMEM/F12 containing 2% horse serum (GE Healthcare), 1× ITS solution (Sigma), and 0.5% Penicillin-Streptomycin. Cardiomyocytes from a healthy donor were obtained from iCell FUJIFILM (catalog no. R1132, R1017). Cells were cultured according to manufacturer's instructions. Briefly, cardiomyocytes were seeded into freshly coated 24-well plates with 0.1% gelatin solution (Millipore Sigma) at a density of 1.8×10^5 cells/well. Plating media was replaced with maintenance media after 2 days. Maintenance media was changed every 2 days until beating was observed. All cells were incubated at 37 °C and 5% CO_2. Experiments with cells were approved by the University of Alberta Health Research Ethics Board.

PMO transfection

The PMOs used in this study are summarized in Table S1 which were derived from our previous publication[27]. The PMOs were obtained from GeneTools, LLC and heated up at 70 °C for 10 min prior to transfection. Myoblasts were transfected with 10 µM PMO in differentiation media along with 6 µM Endoporter (GeneTools, LLC). Random control 25-nt (Gene Tools) was used for mock treatment. The non-treated group contained only Endoporter. Cells were incubated for 2 days with PMO followed by harvesting for RNA extraction. For protein extraction, cells were differentiated for 3 additional days without any PMO.

For all the subsequent imaging and cellular uptake assays, Ac2 was used as the PMO (Table S1). The fluorochrome, carboxyfluorescein, was conjugated to the 3' end of Ac2 and the DG9 peptide (sequence N-YArVRRrGPRGYArVRRrGPRr-C; uppercase: L-amino acids, lowercase: D-amino acids) was conjugated to the 5' end of Ac2. In contrast, for all unlabeled studies, the DG9 peptide was conjugated to the 3' end of Ac2. All in vitro transfections were carried out at 1 µM concentrations for 24 h unless otherwise specified.

Immunocytochemistry

Myoblasts were seeded into 35 mm poly-d-lysine coated dishes (Mattek) at a density of 1×10^5 cells/dish and grown until they were 60% confluent before transfection. For myotubes, cells were differentiated for 7 days with media change every other day until transfection. Cardiomyocytes were seeded at a density of 2.5×10^5 cells/dish into collagen-coated dishes (Mattek) and were grown until beating was observed. All cell types were transfected with 3'-carboxyfluorescein-labeled 1 µM PMO, 20 µM PMO, and 1 µM DG9-PMO in their respective media for 24 h.

To stain for the endosomes, del45 myoblasts and myotubes transfected with DG9-PMO were first washed with PBS followed by 5 min incubation in 4% paraformaldehyde. Then the cells were incubated in 0.1% Triton-X 100 in PBS (PBSTx) for 1 hr at room temperature for antigen retrieval. Next, cells were kept in blocking solution (10% goat serum in PBSTx) for 30 min. Early and late endosomes were stained with Rab5 (Invitrogen PA5-29022) and Rab11 (Invitrogen 71-5300) antibodies, respectively, by using a 1:200 dilution (in blocking solution) for 1 h. After three 5 min PBS washes, secondary antibody staining was done using AlexaFluor™ 594-conjugated goat anti-rabbit IgG secondary antibody (1:1000, A-11037) for 1 h. Finally, cells were washed with PBS and stained with DAPI (Invitrogen). Visualization was done using a Zeiss LSM 710 confocal microscope.

Cell fractionation

For this study, Nunc™ Cell-Culture Treated 24-well plates were coated with 0.1% gelatin solution for 24 h. Del45 myoblasts were seeded at a density of 4×10^4 cells/well and were grown for 2 days. For myotubes, cells were further differentiated for an additional 6 days. Cardiomyocytes (catalog no. R1017) were seeded at a density of 1.27×10^5 cells/well and were grown until beating was observed. Cells were then transfected with 1 µM 3'-carboxyfluorescein-labeled DG9-PMO. Cytoplasmic and nuclear fractionation was carried out using the NE-PER™ Nuclear and Cytoplasmic Extraction Reagents (Thermo Scientific, 78835) and Halt™ Protease Inhibitor Cocktail (Thermo Scientific, 78437), following the manufacturer's guideline. The final solutions containing the nuclear and cytoplasmic fractions were further diluted in 20 and 40 µL water, respectively. Fluorescence intensity was measured in a 96-well black clear bottom plate (Invitrogen) using a SpectraMax M3 plate reader (Ex460/Em520). Finally, western blot analysis was performed using a NuPAGE™ Bis-Tris 4–12% Midi Protein Gel to validate the fractionation. Nuclear and cytoplasmic fractions from del45 myoblasts transfected with DG9-PMO for 2 and 24 h were stained with HDAC2 (Invitrogen 51-5100, 1:500) and GAPDH (Cell Signaling Technology 2118, 1:10,000). Detection was carried out using anti-rabbit IgG (H + L) horseradish peroxidase-conjugated secondary antibodies (Invitrogen 31460, 1:10,000). Throughout the experiment, total nuclear and cytoplasmic protein quantities were measured using a NanoDrop™ Lite Spectrophotometer (Thermo Scientific™) to ensure consistency.

Endocytosis inhibition

Myoblasts were seeded into Nunc™ Cell-Culture Treated 12-well plates at a density of 4×10^4 cells/well and were grown for 2 days. An additional 6 days of differentiation was carried out for myotubes. Cardiomyocytes (catalog no. R1132) were seeded into freshly coated 24-well plates with 0.1% gelatin solution at a density of 1.8×10^5 cells/well and were grown until beating was observed. Cells were pre-treated with endocytosis inhibitors for 30 min. The following inhibitors were used at the highest non-toxic concentration for a given cell type which was derived from a previous study[28]: NaN₃ (10 mM) and 2'-Deoxy-D-Glucose (6 mM) for ATP-depletion, chlorpromazine (CPZ, 3.25 µM for myoblasts and cardiomyocytes, 7.5 µM for myotubes) for clathrin-mediated endocytosis inhibition, nystatin (12.5 µM for myoblasts and cardiomyocytes, 25 µM for myotubes) and genistein (100 µM for myoblasts and cardiomyocytes, 200 µM for myotubes) for caveolae-mediated endocytosis inhibition, and 5-(N-ethyl-N-isopropyl) amiloride (EIPA, 10 µM) for macropinocytosis inhibition. Next, the cells were incubated with fluorescent-tagged DG9-PMO for 4 h in the presence of the inhibitors. The concentrations used for PMO transfection are as follows: 500 nM for myoblasts, 250 nM for myotubes, and 1 µM for cardiomyocytes. Transfections were carried out in DMEM and 0.5% Penicillin-Streptomycin for myoblasts and myotubes, or in maintenance media for cardiomyocytes with a final volume of 500 µL. Cells were washed with PBS after the 4-h incubation. Proliferating cells such

as myoblast and myotubes were further treated with CellTrace™ Calcein Red-Orange (Invitrogen) at a concentration of 1 µg/well for 15 min. Following a PBS wash, cells were lysed with 300 µL GLB buffer (Promega). 100 µL of the cell lysates in a 96-well black clear bottom plate (Invitrogen) were measured for fluorescent intensity using a SpectraMax M3 plate reader (Ex460/Em520 for DG9-PMO and Ex560/Em590 for Calcein Red-Orange). Percentages were calculated after subtracting the baseline (lowest intensity in the non-treated group) from all the groups. To account for the inconsistent cell numbers across the wells, DG9-PMO fluorescent signal was normalized to Calcein Red-Orange.

Confirmation of inhibitors' activity was carried out in del45 myoblasts using known endocytosis markers in a similar fashion. AlexaFluor™ 488-conjugated markers such as human transferrin (8 µg/ml, Invitrogen) for clathrin-mediated endocytosis, cholera toxin B (2 µg/ml, Invitrogen) for caveolae-mediated endocytosis, and Oregon Green™ 488-conjugated dextran (70,000 MW; 250 µg/ml, Invitrogen) for macropinocytosis were incubated in presence of the inhibitors for 2 h. Cells were then washed with PBS and lysed with 300 µL GLB buffer. 100 µL of the cell lysates in a 96-well black clear bottom plate were measured for fluorescent intensity using a SpectraMax M3 plate reader (Ex475/Em525). Percentages were calculated after subtracting the baseline.

Animal treatments

To determine the efficacy and safety of DG9-PMO in vivo, 8 week-old male h*DMD*del45;*mdx* mice (C57BL/6 J background) were used. All the mice were heterozygous for the h*DMD*del45 transgene. For all in vivo experiments, Ac2 was used as the PMO with the peptide conjugated to the 3' end for DG9- and R6G-PMO. First, we evaluated the safety and efficacy of the DG9-PMO. Mice were retro-orbitally injected four times once/week with either saline, PMO (30 mg/kg), or DG9-PMO (30 mg/kg) and euthanized 2 weeks after the treatment for tissue collection. Saline-treated wild-type (WT) served as control. Functional tests were conducted before and 10 days after treatment (Fig. 2a). Blood and urine samples were collected. Body weights were recorded throughout the course of the treatment. All mice were subjected to a 15 mg/kg subcutaneous injection of β-isoproterenol and an intraperitoneal injection of freshly prepared 1% Evans blue dye at 10 ml/kg 24 h before sacrifice. After dissection, tissues were mounted on corks with tragacanth gum and flash-frozen in liquid nitrogen-cooled isopentane.

To assess the changes in cardiac function, 10 week-old male h*DMD*del45;*mdx* mice were treated retro-orbitally twice, once/week, at 30 mg/kg dosage of DG9-PMO or saline. All mice received a subcutaneous injection of 1.5 mg/kg β-isoproterenol every day for 14 days. Echocardiographic imaging was performed before and after treatment. Analysis was done using Vevo LAB version 5.7.1. Blood samples were collected at the end of the treatment for cardiac troponin I (cTnI) analysis. Blood samples were drawn from the tail vein at a volume of 150 µL per mouse. The samples were allowed to sit at room temperature for 30 min before being centrifuged at 15,300 × g (12,000 RPM) for 15 min at 4 °C. The resulting supernatant (serum) was transferred to 1.5 mL tubes and stored at −80 °C. Levels of cTnI in the serum were analyzed commercially by NorthEast BioAnalytical Laboratories LLC. For calculations, samples with optical density (OD) values below the lower limit of the standard curve were assigned a value of 24.55 pg/ml, which corresponds to the lower limit of the standard curve.

For the DG9- vs R6G-PMO study, 8 week-old male h*DMD*del45;*mdx* mice were treated retro-orbitally twice once/week at 30 mg/kg dosage (equivalent to 2190 nmol/kg for DG9-PMO, 2689 nmol/kg for R6G-PMO) followed by euthanasia after 1 week for tissue collection. All injections were conducted under isoflurane anesthesia.

Functional assessment of skeletal and cardiac muscles

Forelimb and total grip strengths were recorded using the Chatillon DFE II grip strength meter (Columbus Instruments). Tests were conducted according to the TREAT-NMD SOP DMD_M.2.2.001 and the average of the three most consistent readings was used. Results were normalized to body weights. The rotarod test was performed using the AccuRotor 4-channel rotarod (Omnitech Electronics, Inc.) following the protocol by Lim et al.[22]. Briefly, mice were placed on a rod rotating at a speed of 5 rpm. The rotation was then accelerated from 5–45 rpm over a span of 300 sec. Fall times were recorded by the software (Fusion ver. 6.5). Three trials were conducted with 15 min breaks in between. The peak fall time was used for analysis. The endurance test was performed according to TREAT-NMD SOP DMD_M.2.1.003 using the Exer 3/6 animal treadmill (Columbus Instruments). Mice were subjected to run on the treadmill with the following program: 5 m/min for 5 min, and 1 m/min increment every minute until exhaustion. Point-of-exhaustion was considered when the mouse did not get back on the treadmill within 10 sec following repeated, gentle nudges. All tests were performed at baseline (pre-treatment) and on day 10 after receiving the final treatment. Tests were performed by blinded personnel.

Echocardiography was performed using the Vevo 3100 with a 40 MHz transducer (MX550S; VisualSonics, Toronto, Canada). Mice were kept on a heating pad with a nose cone delivering 2% isoflurane throughout the procedure. Their temperature was kept between 36.5 to 37.5 °C. Ultrasound gel was applied to the chest of the anesthetized mice, and the ultrasound probe was placed in contact with the gel for scanning, which lasted about 30 min. Throughout the scanning, temperature and heart rate were continuously monitored. M-mode images were used to measure the fractional shortening and left ventricular ejection fraction.

RT-PCR and exon skipping evaluation

Total RNA was extracted from cells and tissue sections (20 µm) using Trizol (Invitrogen) following the manufacturer's instructions. cDNA was synthesized using SuperScript™ IV Reverse Transcriptase (Invitrogen) in accordance with the manufacturer's protocol. 2.5 µM of random hexamers (Invitrogen) were used to synthesize the cDNA from 200 ng of total RNA in a 20 µL reaction. Subsequent amplification of the h*DMD* exon 43-46 region was carried out in a 25 µL reaction containing 5 µL of the cDNA, 1× GoTaq® Green Master Mix (Promega), and 0.4 µM of the forward (GCTCAGGTCGGATTGACATTAT) and the reverse primers (TTTCCAGGTTCAAGTGGGATAC) each. The following program used for the PCR was used: (1) 95 °C, 2 min, (2) 35 cycles of 95 °C, 30 s; 56.5 °C, 30 s; 72 °C, 90 s, (3) 72 °C, 10 min, and (4) 4 °C, hold. All PCR products were run in 2% agarose gels in 1× tris-borate-EDTA buffer. Band intensities were quantified by Image J (NIH). Exon skipping efficiency was calculated from the ratio of the intensity of skipped band and the total intensity of skipped and non-skipped bands.

Protein extraction and western blot

Total protein from cells was extracted using RIPA buffer (Sigma) with cOmplete, Mini, EDTA-free protease inhibitor cocktail (Roche). Total protein from 20 µm tissue sections was collected using SDS lysis buffer containing 10% SDS, 70 mM Tris-HCl (pH 6.7), 5 mM EDTA (pH 8.0), 5% β-mercaptoethanol, and cOmplete protease inhibitor cocktail. Both extractions were carried out according to our previously published protocol[51]. Extracted proteins were quantified using the Pierce™ BCA kit (Thermo Scientific) for cell samples, and the Pierce™ Coomassie (Bradford) kit (Thermo Fisher) for tissue samples.

For western blot, samples were prepared by adding proteins with NuPAGE™ LDS Sample Buffer (Invitrogen; 1× final concentration) and NuPAGE™ Sample Reducing Agent (Invitrogen; 1× final concentration), followed by heating at 70 °C for 10 min. For SDS-PAGE, pre-cast NuPAGE™ 3–8% Tris-Acetate Midi gels (Invitrogen) were used to separate the proteins by running them for 75 min at 150 V. Using a semi-dry blotting system, proteins were transferred onto a PVDF membrane

(Millipore) at 20 V for 70 min. Membranes were then incubated overnight with 2% ECL Prime Blocking Agent (GE Healthcare) while shaking at 4 °C. Post-transfer gels were stained with PageBlue Protein Staining solution (Thermo Scientific) for 1 hr at room temperature to detect myosin heavy chain bands (MyHC) which served as an additional control. After blocking, membranes were cut and incubated with the primary antibodies for 1 hr at room temperature: 1:200 NCL-DYS1 (Leica) for dystrophin, and 1:4,000 anti-desmin (Abcam, ab8592) in blocking agent. After three 10-min PBST (PBS containing 0.05% Tween 20) washes, membranes were incubated with secondary antibodies for 1 hr at room temperature: anti-mouse IgG2a or anti-rabbit IgG (H + L) horseradish peroxidase-conjugated secondary antibodies (Invitrogen A-10685, 31460) for dystrophin and desmin respectively, both 1:10,000 in PBST. Membranes were then washed three times with PBST for 10 min each and bands were detected with ECL Select Detection Reagent (GE Healthcare). Band intensities were quantified using Image Lab™ software, v.6.1 (Bio-Rad), and dystrophin restorations were expressed relative to the intensity of the wild-type samples.

Immunohistochemistry

Frozen tissues were sectioned at 7 μm thickness and placed on poly-L-lysine-coated slides. Sections were thawed and air-dried for 30 min at room temperature before immunostaining. First, the sections were incubated with blocking solution containing PBS with 0.1% Triton-X 100 and 10% goat serum. Sections were then incubated overnight at 4 °C in blocking solution with the following primary antibody: rabbit anti-dystrophin antibody (1:400, ab15277), rat anti-laminin antibody (1:100, ALX-804-190), rabbit anti-Collagen I antibody (1:50, ab34710), or rat anti-mouse CD68 antibody (1:200, MCA1957T). The following day, sections were washed three times with PBS (5 min each), followed by 1 h incubation in PBS with secondary antibody: AlexaFluor™ 488-conjugated goat anti-rabbit IgG secondary antibody (1:2000, A11034), AlexaFluor™ 594-conjugated goat anti-rat IgG secondary antibody for laminin (1:1,000, A11007), or DyLight™ 488-conjugated goat anti-rat IgG secondary antibody for CD68 (1:200, SA510018). Sections were again subjected to three 5 min PBS washes followed by mounting with Vectashield HardSet Antifade Mounting Medium with DAPI (Vector Laboratories). Samples were visualized the next day using a Zeiss LSM 710 confocal microscope (ZEN ver. 13). Quantification was done by blinded personnel. For quantification, cells completely outlined by dystrophin were considered dystrophin-positive.

Tissue histology

Frozen samples were sectioned at 7 μm thickness and placed on poly-L-lysine-coated slides. Sections were first thawed at room temperature for 30 min and then stained with Mayer's hematoxylin (Electron Microscopy Sciences) for 15 min. After washing with running tap water for 15 min, sections were stained with eosin Y (Electron Microscopy Sciences) for 10 min followed by dehydration using a series of concentrated ethanol (70%-90%-99%). Sections were then cleared with a xylene substitute (Thermo Fisher) and mounted with Permount™ (Fisher Chemical). Visualization was done using an Optika B-290TB microscope (Optika Vision Lite ver. 2.13). Subsequent analyses such as centrally nucleated fiber count and Feret's diameter were performed by blinded personnel. Analysis of Feret's diameter was done according to our previously published article[22,52–54]. Briefly, image analysis was conducted using an ImageJ macro adapted from Open-CSAM with custom in-house modifications. The Color Deconvolution 2 plugin facilitated the detection of hematoxylin- and eosin-stained images. Lastly, the images were manually curated to refine fiber boundaries and ensure accurate diameter measurements.

RNA sequencing

Total RNA was extracted from tissue samples using RNeasy Fibrous Tissue Mini Kit (QIAgen). RNA sequencing was done commercially through the Center for Health Genomics and Informatics, University of Calgary. Briefly, samples were assessed via TapeStation assay followed by quantification via DNA and RNA fluorescent assay. Samples with RIN scores greater than 6 were used. Library preparation was performed with 300 ng inputs using NEBNext Ultra II directional RNA kit (New England Biolabs) with poly-A capture module. Assessment of the finished libraries was done via Kapa qPCR assay. Sequencing was performed on an Illumina NovaSeq6000 instrument with 2 × 50 bp read lengths targeting ~33 M read pairs per sample before analysis. RNAseq reads were pseudo-mapped to NCBI RefSeq murine transcript models using Kallisto 0.42.4[55]. Mapping counts were analyzed using Sleuth[56], with three simple binary regression models for each pairwise contrast of dystrophic vs WT, treated vs dystrophic, and treated vs WT. Transcripts that pass the aforementioned regression model with the Wald test p-value < 0.05 after Benjamini-Hochberg multiple testing correction were considered to be differentially expressed (Supplementary Data 1). For some specific transcripts in the treated vs WT comparison, when the expression level was too low in the samples being used for contrast (default filter in Sleuth, 5 reads mapping in each of at least half the samples), expression values were estimated by the addition of the other two contrasts. Enrichment analysis was done using Metascape[38] (Supplementary Data 2).

Toxicology analysis

Blood and urine samples were collected on day 10 post-treatment. Blood was collected from the tail vein at a volume of 100 μL/mouse. Samples were left undisturbed for 30 min at room temperature followed by centrifugation at 15,300 × g (12,000 RPM) for 15 min at 4 °C. The serum was then transferred to a 1.5 mL tube and stored at −80 °C. Serum analysis was done commercially through IDEXX BioAnalytics for the following markers: aspartate aminotransferase (AST), alanine transaminase (ALT), creatine kinase (CK), blood urea nitrogen (BUN), gamma-glutamyl transferase (GGT), and creatinine. Samples having hemolysis index within the normal range were considered for further statistical analysis. For Kidney injury molecule 1 (KIM-1) analysis, 20–50 μL urine was collected per mouse. Samples were centrifuged at 2000 × g for 10 min at 4 °C. Supernatant was collected and stored at −80 °C until further use. KIM-1 analysis was performed using the Mouse KIM-1 ELISA Kit (ab213477) following the manufacturer's protocol.

Statistical analysis and reproducibility

All measurements were obtained from distinct samples, with no repeated measurements conducted except for studies showing changes from the baseline. All statistical tests were carried out using Prism ver. 9 (GraphPad). Analysis such as one-way ANOVA with post-hoc Tukey's or Dunnett's multiple comparisons test, or unpaired two-tailed t-test were conducted as appropriate. P-values less than 0.05 were considered statistically significant. Dystrophin-positive fiber calculations were performed on three independent samples per treatment group to ensure consistency and reliability in the percentage of dystrophin-positive fibers.

Animal husbandry and ethical declaration

The mice were housed in a pathogen-free environment maintained at 22 ± 2 °C with a 14-h light and 10-h dark cycle. They were provided with an irradiated rodent diet (PicoLab® Rodent Diet 20, catalog #5053) ad libitum. Water was deionized, UV-filtered, and supplied in sterilized bottles. All procedures were approved by the University of Alberta Research Ethics Office Animal Care and Use Committee (AUP00000365) and adhered to ARRIVE guidelines. Given that DMD is an X-linked disorder, only male mice were included in this study.

Reporting summary

Further information on research design is available in the Nature Portfolio Reporting Summary linked to this article.

Data availability

The authors declare that all the data supporting the findings of this study are available within the paper and its supplementary information. Source data are provided with this paper. The RNA sequencing data that support the findings of this study are available in Open Science Framework: https://osf.io/37wzb/. Source data are provided with this paper.

References

1. Duan, D., Goemans, N., Takeda, S., Mercuri, E. & Aartsma-Rus, A. Duchenne muscular dystrophy. *Nat. Rev. Dis. Prim.* **7**, 1–19 (2021).
2. Hoffman, E. P., Brown, R. H. & Kunkel, L. M. Dystrophin: The protein product of the duchenne muscular dystrophy locus. *Cell* **51**, 919–928 (1987).
3. Petrof, B. J., Shrager, J. B., Stedman, H. H., Kelly, A. M. & Sweeney, H. L. Dystrophin protects the sarcolemma from stresses developed during muscle contraction. *Proc. Natl. Acad. Sci. USA* **90**, 3710–3714 (1993).
4. Punnoose, A. R. et al. Cardiac disease burden and risk of mortality in hospitalized muscular dystrophy patients. *Pediatr. Cardiol.* **37**, 1290–1296 (2016).
5. Kashyap, N. et al. Prognostic utility of cardiovascular magnetic resonance–based phenotyping in patients with muscular dystrophy. *J. Am. Heart Assoc.* **12**, e030229 (2023).
6. Aartsma-Rus, A., Van Deutekom, J. C. T., Fokkema, I. F., Van Ommen, G.-J. B. & Den Dunnen, J. T. Entries in the Leiden Duchenne muscular dystrophy mutation database: An overview of mutation types and paradoxical cases that confirm the reading-frame rule. *Muscle Nerve* **34**, 135–144 (2006).
7. Lim, K. R. Q., Maruyama, R. & Yokota, T. Eteplirsen in the treatment of Duchenne muscular dystrophy. *DDDT* **11**, 533–545 (2017).
8. Anwar, S. & Yokota, T. Golodirsen for Duchenne muscular dystrophy. *Drugs Today (Barc.)* **56**, 491–504 (2020).
9. Roshmi, R. R. & Yokota, T. Viltolarsen for the treatment of Duchenne muscular dystrophy. *Drugs Today* **55**, 627–639 (2019).
10. Wilton-Clark, H. & Yokota, T. Casimersen for Duchenne muscular dystrophy. *Drugs Today* **57**, 707–717 (2021).
11. Bladen, C. L. et al. The TREAT-NMD DMD global database: analysis of more than 7,000 Duchenne muscular dystrophy mutations. *Hum. Mutat.* **36**, 395–402 (2015).
12. Anthony, K. et al. Biochemical characterization of patients with in-frame or out-of-frame DMD deletions pertinent to exon 44 or 45 skipping. *JAMA Neurol.* **71**, 32–40 (2014).
13. Brogna, C. et al. Upper limb changes in DMD patients amenable to skipping exons 44, 45, 51 and 53: a 24-month study. *Children* **10**, 746 (2023).
14. Brogna, C. et al. Long-term natural history data in Duchenne muscular dystrophy ambulant patients with mutations amenable to skip exons 44, 45, 51 and 53. *PLoS ONE* **14**, e0218683 (2019).
15. Hoy, S. M. Delandistrogene moxeparvovec: first approval. *Drugs* **83**, 1323–1329 (2023).
16. Lek, A., Atas, E., Hesterlee, S. E., Byrne, B. J. & Bönnemann, C. G. Meeting report: 2022 muscular dystrophy association summit on 'safety and challenges in gene transfer therapy'. *J. Neuromuscul. Dis.* **10**, 327–336 (2023).
17. Komaki, H. et al. P.123 a phase I/II study of NS-089/NCNP-02, Exon 44 skipping drug, in patients with Duchenne muscular dystrophy. *Neuromuscul. Disord.* **32**, S99–S100 (2022).
18. Neurology live. *Clinical Potential of AOC 1044 in Treating Duchenne Muscular Dystrophy Amenable to Exon 44 Skipping.* https://www.neurologylive.com/view/clinical-potential-aoc-1044-treating-duchenne-muscular-dystrophy-amenable-exon-44-skipping (2024).
19. Tsoumpra, M. K. et al. Peptide-conjugate antisense based splice-correction for Duchenne muscular dystrophy and other neuro-muscular diseases. *EBioMedicine* **45**, 630–645 (2019).
20. Alter, J. et al. Systemic delivery of morpholino oligonucleotide restores dystrophin expression bodywide and improves dystrophic pathology. *Nat. Med.* **12**, 175–177 (2006).
21. Shah, M. N. A. & Yokota, T. Cardiac therapies for Duchenne muscular dystrophy. *Ther. Adv. Neurol. Disord.* **16**, 17562864231182934 (2023).
22. Lim, K. R. Q. et al. Development of DG9 peptide-conjugated single- and multi-exon skipping therapies for the treatment of Duchenne muscular dystrophy. *Proc. Natl. Acad. Sci. USA* **119**, e2112546119 (2022).
23. Aslesh, T. et al. DG9-conjugated morpholino rescues phenotype in SMA mice by reaching the CNS via a subcutaneous administration. *JCI Insight* **8**, e160516 (2023).
24. Haque, U. S. & Yokota, T. Enhancing antisense oligonucleotide-based therapeutic delivery with dg9, a versatile cell-penetrating peptide. *Cells* **12**, 2395 (2023).
25. Young, C. S., Mokhonova, E., Quinonez, M., Pyle, A. D. & Spencer, M. J. Creation of a novel humanized dystrophic mouse model of duchenne muscular dystrophy and application of CRISPR/Cas9 gene editing therapy. *J. Neuromuscul. Dis.* **4**, 139–145 (2017).
26. Sicinski, P. et al. The molecular basis of muscular dystrophy in the mdx mouse: a point mutation. *Science* **244**, 1578–1580 (1989).
27. Echigoya, Y., Mouly, V., Garcia, L., Yokota, T. & Duddy, W. In silico screening based on predictive algorithms as a design tool for exon skipping oligonucleotides in duchenne muscular dystrophy. *PLoS ONE* **10**, e0120058 (2015).
28. Lehto, T. et al. Cellular trafficking determines the exon skipping activity of Pip6a-PMO in mdx skeletal and cardiac muscle cells. *Nucleic Acids Res.* **42**, 3207–3217 (2014).
29. Spurney, C. F. et al. Preclinical drug trials in the mdx mouse: assessment of reliable and sensitive outcome measures. *Muscle Nerve* **39**, 591–602 (2009).
30. Quinlan, J. G. et al. Evolution of the mdx mouse cardiomyopathy: physiological and morphological findings. *Neuromuscul. Disord.* **14**, 491–496 (2004).
31. Meyers, T. A. et al. Acute AT1R blockade prevents isoproterenol-induced injury in *mdx* hearts. *J. Mol. Cell. Cardiol.* **128**, 51–61 (2019).
32. Yu, L. et al. Small-molecule activation of lysosomal TRP channels ameliorates Duchenne muscular dystrophy in mouse models. *Sci. Adv.* **6**, eaaz2736 (2020).
33. Yue, Y., Skimming, J. W., Liu, M., Strawn, T. & Duan, D. Full-length dystrophin expression in half of the heart cells ameliorates β-isoproterenol-induced cardiomyopathy in mdx mice. *Hum. Mol. Genet.* **13**, 1669–1675 (2004).
34. Strakova, J. et al. Dystrobrevin increases dystrophin's binding to the dystrophin–glycoprotein complex and provides protection during cardiac stress. *J. Mol. Cell. Cardiol.* **76**, 106–115 (2014).
35. Han, W. K., Bailly, V., Abichandani, R., Thadhani, R. & Bonventre, J. V. Kidney injury molecule-1 (KIM-1): a novel biomarker for human renal proximal tubule injury. *Kidney Int.* **62**, 237–244 (2002).
36. Nieves-Rodriguez, S. et al. Transcriptomic analysis of paired healthy human skeletal muscles to identify modulators of disease severity in DMD. *Front. Genet.* **14**, 1216066 (2023).
37. Kamdar, F. et al. Stem cell–derived cardiomyocytes and beta-adrenergic receptor blockade in duchenne muscular dystrophy cardiomyopathy. *J. Am. Coll. Cardiol.* **75**, 1159–1174 (2020).
38. Zhou, Y. et al. Metascape provides a biologist-oriented resource for the analysis of systems-level datasets. *Nat. Commun.* **10**, 1523 (2019).
39. Sarepta Therapeutics. *Community Letter: Update SRP-5051 Program.* https://www.sarepta.com/community-letter-update-srp-5051-program (2024).
40. Betts, C. et al. Pip6-PMO, A new generation of peptide-oligonucleotide conjugates with improved cardiac exon skipping activity for DMD treatment. *Mol. Ther. Nucleic Acids* **1**, e38 (2012).

41. Repellin, M. et al. Repurposing pentamidine using hyaluronic acid-based nanocarriers for skeletal muscle treatment in myotonic dystrophy. *Nanomed.: Nanotechnol. Biol. Med.* **47**, 102623 (2023).

42. Casadei, L. et al. Proteomics-based investigation in C2C12 myoblast differentiation. *Eur. J. Histochem.* **53**, e31 (2009).

43. Hoffman, E. P. et al. Restoring dystrophin expression in Duchenne muscular dystrophy muscle. *Am. J. Pathol.* **179**, 12–22 (2011).

44. Aoki, Y. et al. Highly efficient in vivo delivery of PMO into regenerating myotubes and rescue in laminin-α2 chain-null congenital muscular dystrophy mice. *Hum. Mol. Genet.* **22**, 4914–4928 (2013).

45. Miyatake, S. et al. Scavenger receptor class A1 mediates uptake of morpholino antisense oligonucleotide into dystrophic skeletal muscle. *Mol. Ther. Nucleic Acids* **14**, 520–535 (2019).

46. Aoki, Y. et al. In-frame dystrophin following exon 51-skipping improves muscle pathology and function in the exon 52–deficient mdx mouse. *Mol. Ther.* **18**, 1995–2005 (2010).

47. Watanabe, N. et al. Exon 44 skipping in Duchenne muscular dystrophy: NS-089/NCNP-02, a dual-targeting antisense oligonucleotide. *Mol. Ther. Nucleic Acids* **34**, 102034 (2023).

48. Canonico, F. et al. Focus on the road to modelling cardiomyopathy in muscular dystrophy. *Cardiovasc. Res.* **118**, 1872–1884 (2022).

49. Matsumura, T., Saito, T., Fujimura, H. & Shinno, S. Cardiac troponin I for accurate evaluation of cardiac status in myopathic patients. *Brain Dev.* **29**, 496–501 (2007).

50. Wu, R. P. et al. Cell-penetrating peptides as transporters for morpholino oligomers: effects of amino acid composition on intracellular delivery and cytotoxicity. *Nucleic Acids Res.* **35**, 5182–5191 (2007).

51. Shah, M. N. A. & Yokota, T. Restoring dystrophin expression by skipping exons 6 and 8 in neonatal dystrophic dogs. In *Muscular Dystrophy Therapeutics: Methods and Protocols* (eds. Maruyama, R. & Yokota, T.) 107–124 (Springer US, New York, NY, 2023).

52. Desgeorges, T. et al. Open-CSAM, a new tool for semi-automated analysis of myofiber cross-sectional area in regenerating adult skeletal muscle. *Skelet. Muscle* **9**, 1–12 (2019).

53. Landini, G., Martinelli, G. & Piccinini, F. Colour deconvolution: stain unmixing in histological imaging. *Bioinformatics* **37**, 1485–1487 (2021).

54. Ruifrok, A. C. & Johnston, D. A. Quantification of histochemical staining by color deconvolution. *Anal. Quant. Cytol. Histol.* **23**, 291–299 (2001).

55. Bray, N. L., Pimentel, H., Melsted, P. & Pachter, L. Near-optimal probabilistic RNA-seq quantification. *Nat. Biotechnol.* **34**, 525–527 (2016).

56. Pimentel, H., Bray, N. L., Puente, S., Melsted, P. & Pachter, L. Differential analysis of RNA-seq incorporating quantification uncertainty. *Nat. Methods* **14**, 687–690 (2017).

Acknowledgements

Author contributions

M.N.A.S. and T.Y. conceptualization; M.N.A.S., H.W.C., L.E.S., Radha M., and R.R.R. performed in vivo experiments; M.N.A.S., F.H., B.P., K.R.Q.L. performed in vitro experiments; P.Z. conducted echocardiography; S.A. assisted with dissections and T.A. assisted with KIM1 assay; A.B. provided the del45 cell line; C.S.Y. and M.J.S. provided the h*DMD*del45 mice used to start our colony; S.B. and H.M.M. facilitated the DG9 conjugation; M.N.A.S., Rika M., and G.Y.O. supervision; T.Y. supervision and funding acquisition; M.N.A.S. and T.Y. wrote the manuscript.

Competing interests

T.Y. and Rika M. are cofounders of OligomicsTx Inc., which aims to commercialize antisense technology. The rest of the authors declare no conflict of interest.

Additional information

Supplementary information The online version contains supplementary material available at https://doi.org/10.1038/s41467-025-59494-8.

Correspondence and requests for materials should be addressed to Toshifumi Yokota.

Peer review information *Nature Communications* thanks Arthur Krieg, and the other, anonymous, reviewer(s) for their contribution to the peer review of this work. A peer review file is available.

Reprints and permissions information is available at http://www.nature.com/reprints

Publisher's note Springer Nature remains neutral with regard to jurisdictional claims in published maps and institutional affiliations.